PHOTONICS Research

High power cladding-pumped low quantum defect Raman fiber amplifier

Yang Zhang,[1] Jiangming Xu,[1,4] Junrui Liang,[1] Sicheng Li,[1] Jun Ye,[1,2,3] Xiaoya Ma,[1] Tianfu Yao,[1,2,3] Zhiyong Pan,[1,2,3] Jinyong Leng,[1,2,3] and Pu Zhou[1,5]

[1]College of Advanced Interdisciplinary Studies, National University of Defense Technology, Changsha 410073, China
[2]Nanhu Laser Laboratory, National University of Defense Technology, Changsha 410073, China
[3]Hunan Provincial Key Laboratory of High Energy Laser Technology, National University of Defense Technology, Changsha 410073, China
[4]e-mail: jmxu1988@163.com
[5]e-mail: zhoupu203@163.com

Received 2 November 2023; revised 4 March 2024; accepted 6 March 2024; posted 6 March 2024 (Doc. ID 510057); published 1 May 2024

Heat generated by the quantum defect (QD) in optically pumped lasers can result in detrimental effects such as mode instability, frequency noise, and even catastrophic damage. Previously, we demonstrated that boson-peak-based Raman fiber lasers have great potential in low QD laser generation. But their power scalability and heat load characteristics have yet to be investigated. Here, we demonstrate a boson-peak-based Raman fiber amplifier (RFA) with 815 W output power and a QD of 1.3%. The low heat generation characteristics of this low QD RFA are demonstrated. Both experimental and simulation results show that at this power level, the heat load of the low QD RFA is significantly lower than that of the conventional RFA with a QD of 4.8%. Thanks to its low heat generation characteristics, the proposed phosphosilicate-fiber-based low QD RFA provides an effective solution for the intractable thermal issue in optically pumped lasers, which is of significance in reducing the laser's noise, improving the laser's stability and safety, and solving the challenge of heat removing.

https://doi.org/10.1364/PRJ.510057

1. INTRODUCTION

The boson peak, which refers to the vibrational modes exceeding the Debye predictions in the THz frequency range, is widely observed in thermal measurements, neutron scattering spectra, and Raman scattering spectra of glasses [1–4]. In recent years, the boson peak in vitreous glasses has been extensively studied. Various models are proposed to explain its origin, including phase transition, the Ioffe–Regel limit, the van Hove singularity, shear-elastic heterogeneity, and quasi-localized vibration model [5–9]. Meanwhile, experiments investigating the influence of glass composition, and environment temperature and pressure on the boson peak have been reported in numerous papers [10–12]. While great efforts have been devoted to exploring the nature of the boson peak, the potential applications of the boson peak have drawn little attention. Especially, to the best of our knowledge, the boson peak has rarely been reported for laser emission.

The quantum defect (QD), defined as the relative energy difference between the pump and signal photons in the laser gain process, has always been a troublesome issue in optically pumped lasers. High QD not only limits the power conversion efficiency, but more importantly, it will induce an extra heat load thus degrading the laser's performance. In optically pumped lasers, especially fiber lasers with high power density, heat generated by QD will result in some detrimental effects, such as transverse mode instability, frequency noise, and even catastrophic damage [13–15], making it one of the main challenges that restricts further power scaling and application exploration of fiber lasers [16–18]. Reviewing the power scaling of fiber lasers from the 100 W level to 10 kW level, each momentous power scaling step is accompanied with the dropping of QD, which is gradually decreased from 18.3% to 4.86% [19–21]. In the past two decades, many studies aiming at further reducing the QD of fiber lasers have been reported, most of which are based on rare-earth-doped fibers [22–24]. In 2014, Chang *et al.* realized 5.7 W laser output with a QD of 1.9% through tandem pumping [25]. To further reduce the QD of fiber lasers, AlYahyaei *et al.* utilized ytterbium-doped phosphate fiber as a gain medium and achieved 275 mW laser output with a QD of 0.56% [26]. In recent years, fiber lasers with ultra-low QD or even no QD have been demonstrated via anti-Stokes fluorescence cooling, in which the material is pumped at a photon energy that is lower than the average photon energy of the spontaneous emission [27]. However, this method entails strict demands on the fiber composition and fabrication process, and the power of the reported radiation-balanced fiber lasers is so far limited within watt level [28,29]. In general, the maximum output power of rare-earth-doped

fiber-based low QD (around 1%) lasers is limited at watt level.

Recently, the exploration of the boson peak for laser generation with inherent low QD superiority has been proposed and demonstrated by our group [30,31]. To that end, we have reported hundred-watt-level low QD output in a boson-peak-based core-pumped Raman fiber laser (RFL) [32]. Compared to core-pumping, cladding-pumping allows for higher pump power with low brightness, which is an efficient way to generate high brightness laser beams [33]. And we have proved the feasibility of cladding-pumped low QD RFL [34]. However, the maximum signal output power is 47.7 W, which is limited by the onset of emission at the conventional Raman gain peak. Besides, the heat load and temperature increment characteristics have not been analyzed.

In this paper, we successfully demonstrate a cladding-pumped low QD Raman fiber amplifier (RFA) with 815 W output power. To prove its advantage in low heat generation, we compare the temperature increment of the low QD RFA with a conventional RFA with a QD of 4.8% using the same fiber. Both experimental and simulation results show that at this power level, the heat load of the low QD RFA is significantly lower than that of the conventional RFA. The low heat generation characteristics is of significance in reducing the laser's noise, improving the laser's stability and safety, and solving the challenge of heat removing.

2. PRINCIPLE AND EXPERIMENTAL SETUP

The Raman effect, in which the energy transfers between the incident light and phonons in the scattering medium, has been widely utilized in fiber lasers for the unique advantages of having a broadband gain spectrum, no photon darkening, and flexible wavelength tunability [35–38]. The Boson peak, as a kind of transverse phonon, can be utilized to provide Raman gain. The intensity of the boson peak differs in optical fibers with different materials. It has been shown that phosphorus doping can significantly enhance the intensity of the boson peak in common silica fiber [12]. Hence, we chose phosphosilicate fiber as the Raman gain medium. Figure 1 displays the measured Raman gain spectrum of the phosphosilicate fiber we used. Compared to the common silica fiber with a main Raman peak at around 13.2 THz, the phosphosilicate fiber has two extra Raman peaks. One arises from vibrational modes of the phosphorus-oxygen double bond at a frequency shift of ~40 THz, and it is useful for extending the wavelength range of RFLs [39,40]. The other one is the boson peak at a frequency shift of ~3.6 THz. By using this peak to provide Raman gain, we built a cladding-pumped low QD RFA.

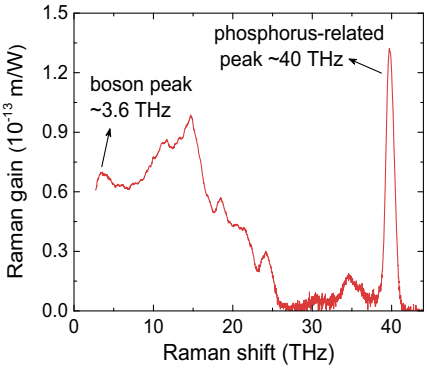

Fig. 1. Measured Raman gain spectrum of the utilized phosphosilicate fiber.

The schematic of the low QD RFA is shown in Fig. 2. It consists of a 1080 nm seed laser, a circulator, two high power pump sources, a combiner, and a section of phosphosilicate fiber. The seed laser is a 1080 nm fiber oscillator with a 50 W output power and a core diameter of 10 μm. To protect the seed laser from backward scattered light, a high power circulator with 10 μm core fiber pigtails is spliced after the seed laser. The pump sources are two high power tunable ytterbium-doped fiber lasers [41], which can deliver a total of 1.6 kW output power over a tuning range of 1055–1075 nm. To match the frequency shift of the boson peak, the pump wavelength is set at 1066 nm. The output fibers of the two pump sources have the same core diameter of 20 μm. The Raman gain fiber is a length of specially designed triple-clad phosphosilicate fiber, whose core, inner-cladding, and outer-cladding diameters are 29 μm, 56 μm, and 130 μm, respectively. The core area is doped with phosphorus, which could induce a strong boson peak in its Raman gain spectrum [12]. The inner-cladding area is doped with germanium. The refractive index profile of the phosphosilicate fiber is shown in the inset picture in Fig. 2. The numerical apertures of the core and inner-cladding area are 0.08 and 0.17, respectively. The fiber is coiled on an aluminum barrel with a radius of 14 cm, and the measured transmission loss of the core is 1.4 dB/km at 1080 nm. The outputs from the seed laser and pump sources are coupled into the phosphosilicate fiber through a specially designed (2 + 1) × 1 pump/signal combiner. The core/cladding diameters of the input signal fiber are 10/125 μm, and the numerical apertures are 0.08/0.46. The core/cladding diameters of the input pump fibers are 20/130 μm, and the numerical apertures are 0.08/0.46. The output fiber is the 29/26/130 triple-clad phosphosilicate fiber we used. The signal coupling efficiency from the signal port to the core area is 60%. The pump coupling efficiencies of the two pump ports to the inner-cladding area are 98.2% and 98.1%. The 1080 nm signal in the core area is amplified by the Raman gain arising from the boson peak. The light from the phosphosilicate fiber is exported by a homemade quartz block head. The total output power is measured by a power meter with power capacity of 5 kW. To precisely measure the output spectrum, we use a piece of multimode fiber with core diameter of 105 μm and numerical aperture of 0.22 to collect the reflected light from the power meter and deliver it to the optical spectrum analyzer [42].

3. EXPERIMENTAL RESULTS

To get higher output power, a cutback experiment was performed by reducing the fiber length from 500 m to 100 m. The maximum signal output power and the corresponding normalized output spectra for different fiber lengths are displayed in Fig. 3(a). To be noted, there is broadband amplified spontaneous noise in the spectral range of 1070–1100 nm, which

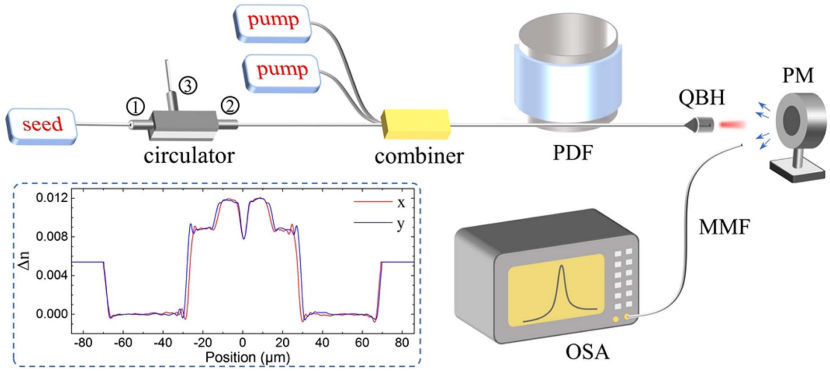

Fig. 2. Schematic of the high power low quantum defect Raman fiber amplifier. PF, phosphosilicate fiber; QBH, quartz block head; PM, power meter; MMF, multimode fiber; OSA, optical spectrum analyzer. Inset, refractive index profile of the phosphosilicate fiber.

might originate from the spontaneous noise amplified by the Raman gain in the phosphosilicate fiber. To properly analyze the output power characteristics, we have subtracted the amplified spontaneous noise from the net signal value. As the fiber is shortened, the signal power increases significantly, due to lower transmission loss and higher threshold power for spontaneous Raman generation at 13.2 THz. The highest output power of 815 W is achieved with a 150-m-long fiber. However, as the fiber is shortened, more pump light remains unconverted. At 100 m, so much of the pump passes unconverted that we are only able to achieve 523 W signal output power using all of the available pump power. The spectral and power evolution characteristics of this 150 m RFA are depicted in Figs. 3(b) and 3(c), respectively. At low pump power, much of the pump remains unconverted in the RFA due to its relatively low intensity, and the residual pump power exceeds the signal power. As the pump power increases, more of it is converted into 1080 nm signal until, at 1235 W, the residual pump power begins to decrease with increasing pump injection, and the 1080 nm signal dominates. When the pump power is increased to 1568 W, the signal power reaches its maximum of 815 W, the spontaneous Raman generation at 13.2 THz reaches 17.2 W, and 529 W pump power remains unconverted. The corresponding optical conversion efficiency is 48.8%. Further power scaling is restricted by the limited pump conversion efficiency and spontaneous Raman generation at 13.2 THz.

To demonstrate the low QD RFA's advantage in low heat generation, we measure the coating temperature of the gain fiber with an infrared thermal imager and compare it with a conventional RFA. The conventional RFA is built from the same gain fiber and pump source. We only replace the 1080 nm seed laser with a 1120 nm fiber oscillator, which has the same

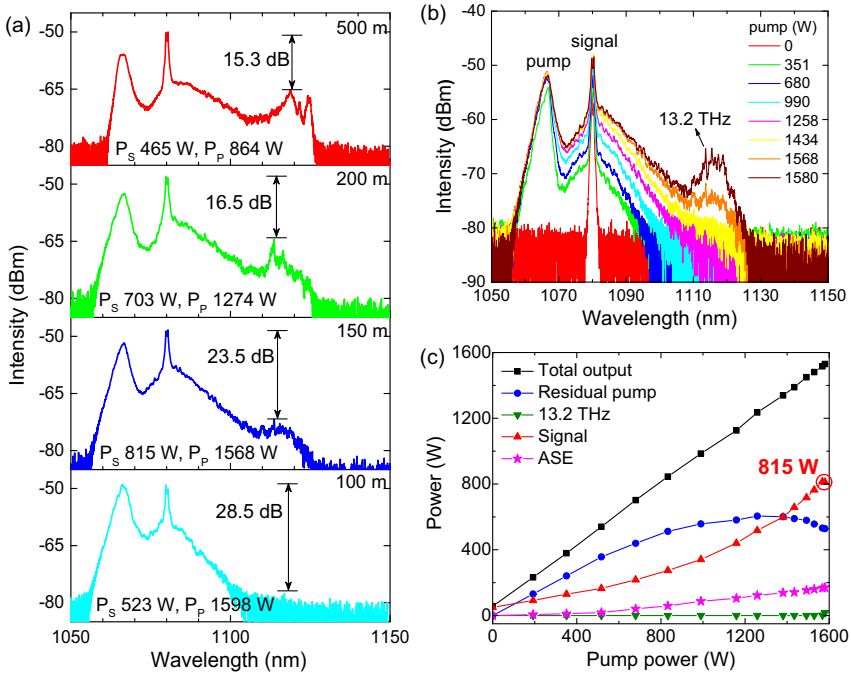

Fig. 3. (a) Maximum output powers and corresponding output spectra at different fiber lengths. (b) Spectral evolution and (c) power evolution characteristics of the low QD RFA under an optimized fiber length of 150 m. ASE, amplified spontaneous emission.

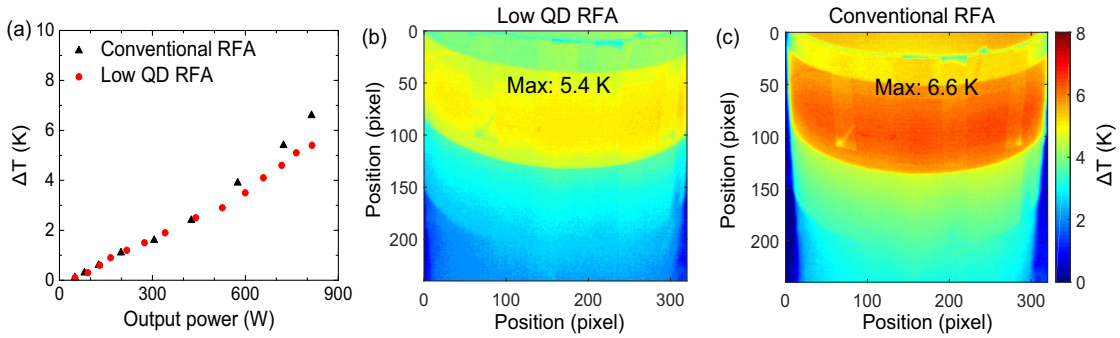

Fig. 4. (a) Highest temperature increment measured at the fiber coating of each RFA as a function of output power. (b) Thermal image of the gain fiber in the low QD RFA at 815 W signal power. (c) Thermal image of the gain fiber in the conventional RFA at 813 W signal power.

structure and output power. And the QD between the 1066 nm pump source and 1120 nm Raman signal is 4.82%, more than three times that of the low QD RFA. Figure 4(a) shows the highest temperature increment measured at the fiber coating of each RFA as a function of output power. When the output power is below 400 W, the temperature difference between the two RFAs is negligible. Above 400 W, the temperature increment in the low QD RFA is clearly lower than that of the conventional RFA, for reasons which will be explained in Section 4.B. At the low QD RFA's maximum signal power of 815 W, the fiber coating temperature reaches a maximum of 5.4 K above ambient, whereas it reaches a maximum of 6.6 K above ambient in the conventional RFA operating at the same signal power. The corresponding thermal images of the two RFAs are displayed in Figs. 4(b) and 4(c), respectively, with the low QD RFA showing an 18% reduction of the temperature increment. This result demonstrates the advantage of our low QD RFA in reducing heat generation, which is further confirmed by our simulation results described in Section 4.B.

4. THEORETICAL ANALYSIS

A. Power Evolution Analysis

In RFA, propagation loss and the QD of the Raman conversion process are the main sources of heat load. Consequently, we must determine the power evolution characteristics along the fiber length before we can calculate the heat distribution. In order to calculate the power evolution characteristics in the cladding-pumped low QD RFA, we employ a modified power balanced model based on the one described in Ref. [43], where the pump directly provides gain at both the 1080 nm signal wavelength and the 1118.5 nm first order Stokes wavelength, and the 1080 nm signal also provides gain at 1118.5 nm. The power evolution process can then be written as

$$\frac{dP_0}{dz} = -\alpha_0 P_0 - \frac{g_{R01}}{A_{\text{clad}}}\frac{\lambda_1}{\lambda_0}P_0P_1 - \frac{g_{R02}}{A_{\text{clad}}}\frac{\lambda_2}{\lambda_0}P_0P_2, \quad (1)$$

$$\frac{dP_1}{dz} = -\alpha_1 P_1 + \frac{g_{R01}}{A_{\text{clad}}}P_0P_1 - \frac{g_{R12}}{A_{\text{core}}}\frac{\lambda_2}{\lambda_1}P_1P_2, \quad (2)$$

$$\frac{dP_2}{dz} = -\alpha_2 P_2 + \frac{g_{R12}}{A_{\text{core}}}P_1P_2 + \frac{g_{R02}}{A_{\text{clad}}}P_0P_2, \quad (3)$$

where the lower indices 0, 1, 2 refer to the pump, 1080 nm signal, and 1118.5 nm Stokes spontaneous Raman generation, respectively. P is the power, α is the attenuation coefficient, λ is the wavelength, g_{R01} and g_{R02} are the Raman gain coefficients at 1080 nm and 1118.5 nm, respectively, relative to the pump, and g_{R12} is the Raman gain coefficient at 1118.5 nm relative to the 1080 nm signal. A_{core} and A_{clad} are the effective mode areas of the core and inner cladding, respectively.

The fiber parameters used in the numerical simulation are summarized in Table 1. The fiber length is set to 150 m. Considering the signal coupling efficiency of the coupler, the input signal power at 1080 nm is set at 40 W with a 50 W seed laser injected. Considering the amplified spontaneous emission in the pump, the initial power of 1118.5 nm first order Stokes light is set to be a millionth of the pump power at 1066 nm [41]. The calculated output power evolution results are shown in Fig. 5(a). The black, red, blue, and green lines represent the total output power, 1080 nm signal power, residual pump power, and Stokes spontaneous Raman generation at 13.2 THz, respectively.

At maximum pump power of 1.6 kW, the signal power reaches 958.6 W, the spontaneous Raman generation at 13.2 THz reaches 18.6 W, and 570.5 W of pump power remains unconverted. The corresponding experimental results are also displayed in the same figure. Since the broadband amplified spontaneous noise in the spectral range of 1070–1100 nm is not considered in the simulation, the simulated power evolution results differ from the experimental data. Figure 5(b) shows the calculated longitudinal distribution of the laser power in the low QD RFA at maximum pump power of 1.6 kW. The signal power does not begin to overtake the pump power until the last fifth of the fiber, where most of the QD heating is generated.

Table 1. Parameter Values in Power Evolution Analysis

Parameter	Value
$\lambda_0, \lambda_1, \lambda_2$	1066, 1080, 1118.5 nm
$\alpha_0, \alpha_1, \alpha_2$	1.48, 1.40, 1.22 dB/km
$g_{R01}, g_{R02}, g_{R12}$	7×10^{-14}, 9.87×10^{-14}, 8×10^{-14} m/W
$A_{\text{core}}, A_{\text{clad}}$	1065.35, 3972.59 μm^2

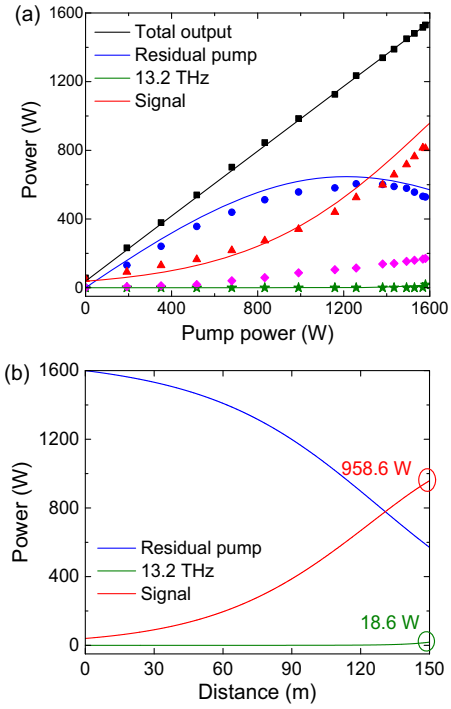

Fig. 5. (a) Calculated output power evolution characteristics in the low QD RFA; the scattered points are the corresponding experimental results. (b) Calculated longitudinal power distribution of the low QD RFA at pump power of 1.6 kW.

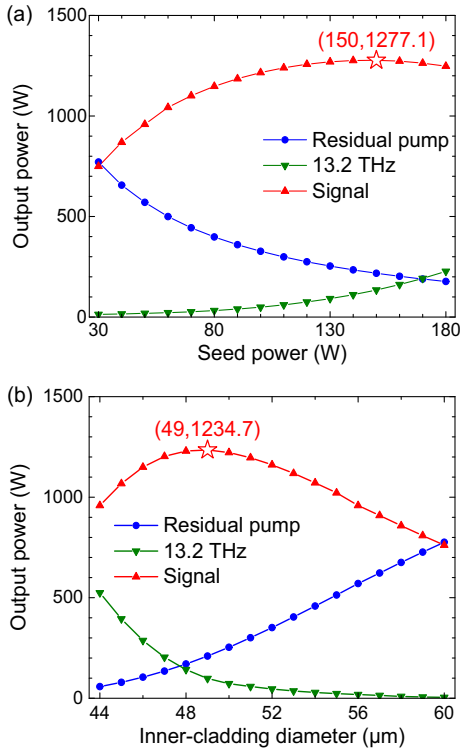

Fig. 6. Output powers of Raman signal, residual pump, and spontaneous Raman generation at (a) different seed powers and (b) different inner-cladding diameters.

In a cladding pumped Raman fiber amplifier, the seed power and cladding-to-core area ratio of the fiber can influence the power conversion efficiency [44,45]. To investigate the further power scalability of the proposed low QD Raman fiber amplifier, we simulate its output power characteristics at different seed powers and cladding-to-core area ratios. First, we keep the core and inner-cladding diameters unchanged and increase the seed power from 30 W to 180 W. To be noted, the signal power injected into the fiber core is 80% of the input seed power considering the 80% signal coupling efficiency of the combiner. Figure 6(a) displays the output power of the Raman signal, residual pump, and spontaneous Raman generation at 13.2 THz under different seed powers. Increasing the seed power will lead to less residual pump but more spontaneous Raman emission at 13.2 THz. The output Raman signal power reaches the maximum of 1277.1 W with 150 W seed power. Second, we keep the seed power at 50 W, and vary the cladding-to-core area ratio. The core/cladding ratio of the fiber is adjusted by reducing the inner-cladding diameter from 60 μm to 44 μm while keeping the core diameter at 29 μm. The simulated results are shown in Fig. 6(b). Reducing the inner-cladding diameter will lead to less residual pump but more spontaneous Raman emission at 13.2 THz. When the inner-cladding diameter is reduced to 49 μm, the output Raman signal power reaches the maximum of 1234.7 W. The further power increase is limited by the spontaneous Raman emission at 13.2 THz. In our experiment, the maximum output power of the seed laser is 50 W and the inner-cladding diameter is 56 μm; the output signal power is mainly limited by insufficient Raman conversion. In future work, we will optimize the cladding-to-core area ratio of the Raman fiber and build a seed laser with higher output power to further increase the conversion efficiency and output power of the proposed low QD Raman amplifier.

B. Heat Analysis

Using the calculated longitudinal power distribution as shown in Fig. 5(b), we can reveal the heat load and temperature distribution characteristics of the two RFAs (see Appendix A for more details). The fiber parameters used in our heat distribution analysis are summarized in Table 2 and the calculated results are shown in Fig. 7.

Figure 7(a) displays the longitudinal heat load distribution in the two RFAs operating at the same signal power of 1 kW. Near the input port of the fiber, much of the pump remains unconverted and the heat load is mainly generated by the propagation loss; due to the relatively higher pump power, the heat load in the low QD RFA is slightly higher than that of the conventional RFA. As the pump wave propagates along

Table 2. Parameter Values in Heat Analysis

Parameter	Value
r_1, r_2, r_3, r_4	14.5, 28, 65, 125 μm
$\kappa_1, \kappa_2, \kappa_3, \kappa_4$ [46]	1.38, 1.38, 1.38, 0.2 W/(m · K)
T_0	298.15 K
h	100 W/(m^2 · K)

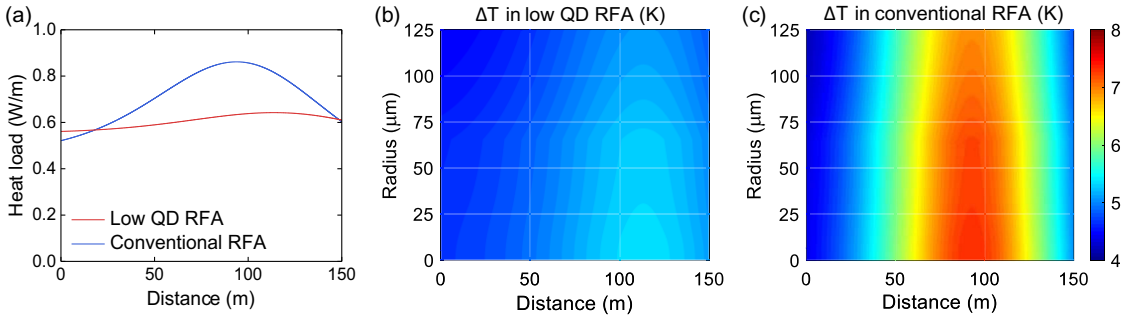

Fig. 7. (a) Longitudinal heat load distribution along the phosphosilicate fiber in the two RFAs. (b) Temperature increment distribution in the low QD RFA and (c) conventional RFA operating at the same signal power of 1 kW.

the fiber, more of it is converted into the Raman signal and QD-induced heat load increases sharply. As a result, the heat load in the conventional RFA exceeds the low QD RFA due to higher QD. In the low QD RFA, the heat load reaches a maximum of 0.64 W/m at a position of 113 m, whereas in the conventional QD RFA, the maximum heat load is 0.86 W/m at a position of 92 m. And the integrated heat load in the low QD RFA is 91 W, 16% lower than the 108 W in the conventional RFA. Figures 7(b) and 7(c) show the temperature increment distributions along the phosphosilicate fiber in the two RFAs operated at 1 kW signal power. Along the longitudinal direction, the temperature variation exhibits a similar trend to the heat load. In the low QD RFA, the core temperature increment varies from 4.67 K to 5.36 K, while in the conventional RFA, the core temperature increment varies from 4.34 K to 7.19 K. Along the transverse direction, the temperature decreases with increasing radius. In the conventional RFA, the maximum temperature difference between the core and cladding is 0.39 K, whereas in the low QD RFA, the value is 0.28 K. The temperature increment in the low QD RFA is clearly lower than that of the conventional RFA.

To better understand the low QD RFA's advantage in reducing heat generation, we calculate the QD-induced heat load, propagation-loss-induced heat load, and total heat load of the two RFAs as functions of output power. The simulation results are plotted in Fig. 8(a). The solid line and dashed line represent the integrated heat load of the low QD RFA and the conventional RFA, respectively. The red, green, and blue lines represent the total heat load, propagation-loss-induced heat load, and QD-induced heat load, respectively. In the low QD RFA, its QD-induced heat load is always about one third of the conventional RFA's due to the low QD, whereas its propagation-loss-induced heat load is slightly higher due to the higher pump power. When the signal output power is below 400 W, the total heat loads of the two RFAs are almost the same.

Above 400 W, the total heat load of the conventional RFA exceeds the low QD RFA due to the rapidly increased QD-induced heat load. When the signal output power reaches 1 kW, the total heat load of the conventional RFA is 108 W, whereas in the low QD RFA, it is 91 W. As signal power continues to increase, the heat load gap between the two RFAs becomes larger. To further explore the low QD RFA's potential

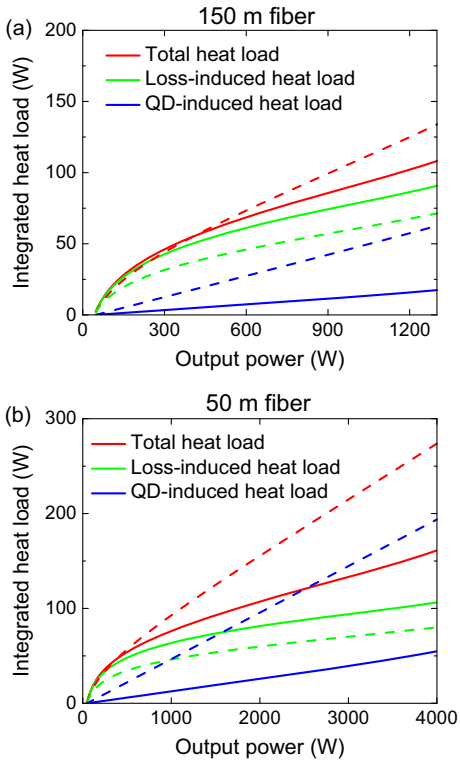

Fig. 8. Integrated heat load in the two RFAs as a function of output power with (a) 150 m and (b) 50 m Raman fiber. (The solid line and dashed line represent the integrated heat load of the low QD RFA and the conventional RFA, respectively. The red, green, and blue lines represent the total heat load, propagation-loss-induced heat load, and QD-induced heat load, respectively.)

in low heat generation, we cut the fiber length into 50 m, where up to 4 kW signal power can be obtained, and calculate the heat loads of the two RFAs. The simulation results are shown in Fig. 8(b). In the conventional RFA, QD-induced heat load begins to dominate after the signal output power exceeds 1 kW, while in the low QD RFA, the propagation-loss-induced heat load is always the dominant source of heat due to the extremely low QD. At 4 kW signal output power, the total heat load in the low QD RFA is 161 W, about 41% lower than the

274 W in the conventional RFA. If the propagation loss of the phosphosilicate fiber can be reduced to the same level as common silica fiber, about 1.2 dB/km [47], the total heat load in the low QD RFA can be further reduced to 142 W.

5. CONCLUSION

In conclusion, we demonstrate 815 W laser output with a QD of 1.3% in a boson-peak-based low QD RFA. At maximum output power, the highest temperature increment in the low QD RFA is 5.4 K, 18% lower than that of the conventional RFA with a QD of 4.8%. The calculated integrated heat load at 1 kW output power is 91 W, 16% lower than that of the conventional RFA. Further simulation reveals that the low QD RFA's advantage of low heat load becomes more prominent with the increase of output power. At 4 kW output power, the integrated heat load of the low QD RFA is 41% lower than that of the conventional RFA. The successful demonstration of the high power low QD laser output with low heat load is of great significance in solving the intractable thermal issues of high power lasers.

APPENDIX A: TEMPERATURE DISTRIBUTION ANALYSIS

Due to the isotropic cylindrical structure, the temperature distribution in the fiber can be obtained from the steady heat equation as follows [46]:

$$\nabla^2 T + \frac{Q}{\kappa} = 0, \tag{A1}$$

where T is the temperature, Q is the generated heat density per unit volume, and κ is the thermal conductivity. As shown in Fig. 9, in the triple-clad phosphosilicate fiber, power losses originated from transmission loss in the inner-cladding area and Raman conversion process in the core area will all be converted into heat. Consequently, heat is generated in the core and inner-cladding area, and the thermal conduction equations in the triple-clad phosphosilicate fiber can be written as follows:

$$\frac{1}{r}\frac{\partial}{\partial r}\left(r\frac{\partial T_1(r)}{\partial r}\right) + \frac{Q_1}{\kappa_1} = 0, \qquad 0 \le r \le r_1, \tag{A2}$$

$$\frac{1}{r}\frac{\partial}{\partial r}\left(r\frac{\partial T_2(r)}{\partial r}\right) + \frac{Q_2}{\kappa_2} = 0, \qquad r_1 \le r \le r_2, \tag{A3}$$

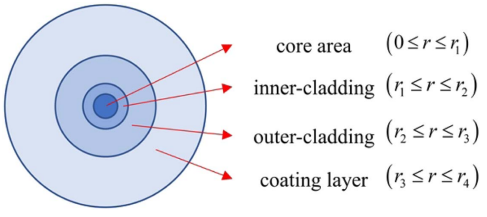

Fig. 9. Cross section of the triple-clad phosphosilicate fiber.

$$\frac{1}{r}\frac{\partial}{\partial r}\left(r\frac{\partial T_3(r)}{\partial r}\right) = 0, \qquad r_2 \le r \le r_3, \tag{A4}$$

$$\frac{1}{r}\frac{\partial}{\partial r}\left(r\frac{\partial T_4(r)}{\partial r}\right) = 0, \qquad r_3 \le r \le r_4, \tag{A5}$$

where r is the radius, and $T_j(r)$ $(j = 1, 2, 3, 4)$ are the temperature distribution functions in different layers. κ_1 and κ_2 are the thermal conductivity of the core and inner-cladding area, respectively. Q_1 and Q_2 are the heat density generated in the core and inner-cladding area, which can be calculated with the power distribution data as follows:

$$Q_1 = \frac{\alpha_0 P_0}{A_{\text{clad}}} + \frac{\alpha_1 P_1}{A_{\text{core}}} + \frac{\alpha_2 P_2}{A_{\text{core}}} + \frac{g_{R01}}{A_{\text{clad}} A_{\text{core}}}\frac{\lambda_1 - \lambda_0}{\lambda_1} P_0 P_1 + \frac{g_{R02}}{A_{\text{clad}} A_{\text{core}}}\frac{\lambda_2 - \lambda_0}{\lambda_2} P_0 P_2 + \frac{g_{R02}}{A_{\text{core}} A_{\text{core}}}\frac{\lambda_2 - \lambda_1}{\lambda_2} P_1 P_2, \tag{A6}$$

$$Q_2 = \frac{\alpha_0 P_0}{A_{\text{clad}}}. \tag{A7}$$

According to Fourier's law of thermal conduction and Newton's law of cooling, the boundary conditions under steady state can be expressed as follows:

$$T_i(r_i) = T_{i+1}(r_i), \qquad i = 1, 2, 3, \tag{A8}$$

$$\kappa_i T_i'(r_i) = \kappa_{i+1} T_{i+1}'(r_i), \qquad i = 1, 2, 3, \tag{A9}$$

$$T_4'(r_4) = \frac{h}{\kappa_4}(T_0 - T_4(r_4)), \tag{A10}$$

where T_0 is the coolant temperature, and h is the convective heat transfer coefficient. Based on the heat conduction model above, the temperature distribution along the fiber cross section can be obtained:

$$T_1(r) = T_0 + \frac{Q_1(r_1^2 - r^2)}{4\kappa_1} - \frac{(Q_1 - Q_2)r_1^2}{2\kappa_2}\ln r_1 + \left(\frac{(Q_1 - Q_2)r_1^2}{2\kappa_2} - \frac{Q_1 r_1^2 + Q_2(r_2^2 - r_1^2)}{2\kappa_3}\right)\ln r_2 + \frac{Q_2(r_2^2 - r_1^2)}{4\kappa_2} + (Q_1 r_1^2 + Q_2(r_2^2 - r_1^2)) \times \left(\frac{1}{2hr_4} + \frac{\ln r_4}{2\kappa_4} + \frac{\ln r_3}{2\kappa_3} - \frac{\ln r_3}{2\kappa_4}\right), \qquad 0 \le r \le r_1, \tag{A11}$$

$$T_2(r) = T_0 + \frac{Q_2(r_2^2 - r^2)}{4\kappa_2} - \frac{(Q_1 - Q_2)r_1^2}{2\kappa_2}\ln r + \left(\frac{(Q_1 - Q_2)r_1^2}{2\kappa_2} - \frac{Q_1 r_1^2 + Q_2(r_2^2 - r_1^2)}{2\kappa_3}\right)\ln r_2 + (Q_1 r_1^2 + Q_2(r_2^2 - r_1^2)) \times \left(\frac{1}{2hr_4} + \frac{\ln r_4}{2\kappa_4} + \frac{\ln r_3}{2\kappa_3} - \frac{\ln r_3}{2\kappa_4}\right), \qquad r_1 \le r \le r_2, \tag{A12}$$

$$T_3(r) = T_0 - \frac{Q_1 r_1^2 + Q_2(r_2^2 - r_1^2)}{2\kappa_3}\ln r + (Q_1 r_1^2 + Q_2(r_2^2 - r_1^2))\left(\frac{1}{2hr_4} + \frac{\ln r_4}{2\kappa_4} + \frac{\ln r_3}{2\kappa_3} - \frac{\ln r_3}{2\kappa_4}\right), \quad r_2 \le r \le r_3, \tag{A13}$$

$$T_4(r) = T_0 - \frac{Q_1 r_1^2 + Q_2(r_2^2 - r_1^2)}{2\kappa_4}\ln r + (Q_1 r_1^2 + Q_2(r_2^2 - r_1^2))\left(\frac{1}{2hr_4} + \frac{\ln r_4}{2\kappa_4}\right), \quad r_3 \le r \le r_4. \tag{A14}$$

Funding. National Postdoctoral Program for Innovative Talents (BX20190063); National Natural Science Foundation of China (61635005, 61905284, 62305391).

Acknowledgment. We are grateful to Sen Guo, Cong Zhou, Tao Wang, Bo Ren, Pengfei Ma, and Yisha Chen for their help with this work.

Disclosures. The authors declare no conflicts of interest.

Data Availability. Data underlying the results presented in this paper are not publicly available at this time but may be obtained from the authors upon reasonable request.

REFERENCES

1. T. Nakayama, "Boson peak and terahertz frequency dynamics of vitreous silica," Rep. Prog. Phys. **65**, 1195–1242 (2002).
2. J. Bünz, T. Brink, and K. Tsuchiya, "Low temperature heat capacity of a severely deformed metallic glass," Phys. Rev. Lett. **112**, 135501 (2014).
3. S. Ren, H. Zong, X. Tao, *et al.*, "Boson-peak-like anomaly caused by transverse phonon softening in strain glass," Nat. Commun. **12**, 5575 (2021).
4. M. G. Jiménez, T. Barnard, B. A. Russell, *et al.*, "Understanding the emergence of the boson peak in molecular glasses," Nat. Commun. **14**, 215 (2023).
5. T. S. Grigera, V. Martin-Mayor, G. Parisi, *et al.*, "Phonon interpretation of the 'boson peak' in supercooled liquids," Nature **422**, 289–292 (2003).
6. H. Tanaka and H. Shintani, "Universal link between the boson peak and transverse phonons in glass," Nat. Mater. **7**, 870–877 (2008).
7. A. I. Chumakov, G. Monaco, A. Monaco, *et al.*, "Equivalence of the boson peak in glasses to the transverse acoustic van Hove singularity in crystals," Phys. Rev. Lett. **106**, 225501 (2011).
8. M. Baggioli and A. Zaccone, "Universal origin of boson peak vibrational anomalies in ordered crystals and in amorphous materials," Phys. Rev. Lett. **122**, 145501 (2019).
9. Y. Hu and H. Tanaka, "Origin of the boson peak in amorphous solids," Nat. Photonics **18**, 669–688 (2022).
10. V. K. Malinovsky and A. P. Sokolov, "The nature of boson peak in Raman scattering in glasses," Solid State Commun. **57**, 757–761 (1986).
11. J. Schroeder, W. Wu, J. L. Apkarian, *et al.*, "Raman scattering and boson peaks in glasses: temperature and pressure effects," J. Non-Cryst. Solids **349**, 88–97 (2004).
12. H. E. Hamzaoui, M. Bouazaoui, and B. Capoen, "Raman investigation of germanium-and phosphorus-doping effects on the structure of sol–gel silica-based optical fiber preforms," J. Mol. Struct. **1099**, 77–82 (2015).
13. C. Jauregui, C. Stihler, and J. Limpert, "Transverse mode instability," Adv. Opt. Photon. **12**, 429–484 (2020).
14. C. Jauregui, J. Limpert, and A. Tünnermann, "High-power fibre lasers," Nat. Photonics **7**, 861–867 (2013).
15. M. N. Zervas, "Transverse-modal-instability gain in high power fiber amplifiers: effect of the perturbation relative phase," APL Photon. **4**, 022802 (2019).
16. D. J. Richardson, J. Nilsson, and W. A. Clarkson, "High power fiber lasers: current status and future perspectives [Invited]," J. Opt. Soc. Am. B **27**, B63–B92 (2010).
17. J. Nilsson and D. N. Payne, "High-power fiber lasers," Science **332**, 921–922 (2011).
18. X. Chen, T. Yao, L. Huang, *et al.*, "Functional fibers and functional fiber-based components for high-power lasers," Adv. Fiber. Mater. **5**, 59–106 (2023).
19. V. Dominic, S. MacCormack, R. Waarts, *et al.*, "110 W fibre laser," Electron. Lett. **35**, 1158–1160 (1999).
20. Y. Jeong, J. K. Sahu, D. N. Payne, *et al.*, "Ytterbium-doped large-core fibre laser with 1 kW of continuous-wave output power," Electron. Lett. **40**, 470–472 (2004).
21. E. Stiles, "New developments in IPG fiber laser technology," in *5th International Workshop on Fiber Lasers* (2009).
22. S. Matsubara, K. Uno, Y. Nakajima, *et al.*, "Extremely low quantum defect oscillation of ytterbium fiber laser by laser diode pumping at room temperature," in *Advanced Solid-State Photonics*, OSA Technical Digest Series (CD) (Optica, 2007), paper TuB4.
23. T. Yao, J. Ji, and J. Nilsson, "Ultra-low quantum-defect heating in ytterbium-doped aluminosilicate fibers," J. Lightwave Technol. **32**, 429–434 (2014).
24. N. Yu, M. Cavillon, C. Kucera, *et al.*, "Less than 1% quantum defect fiber lasers via ytterbium-doped multicomponent fluorosilicate optical fiber," Opt. Lett. **43**, 3096–3099 (2018).
25. Y. Chang, T. Yao, H. Jeong, *et al.*, "3% thermal load measured in tandem-pumped ytterbium-doped fiber amplifier," in *CLEO: 2014*, OSA Technical Digest (online) (Optica, 2014), paper STh4N.7.
26. K. AlYahyaei, X. Zhu, L. Li, *et al.*, "Ultralow-quantum-defect single-frequency fiber laser," Opt. Lett. **48**, 3817–3820 (2023).
27. N. Yu, K. V. Desai, A. E. Mironov, *et al.*, "Reduced quantum defect in a Yb-doped fiber laser by balanced dual-wavelength excitation," Appl. Phys. Lett. **119**, 141105 (2021).
28. J. M. Knall, M. Engholm, T. Boilard, *et al.*, "Radiation-balanced silica fiber amplifier," Phys. Rev. Lett. **127**, 013903 (2021).
29. J. Knall, M. Engholm, T. Boilard, *et al.*, "Radiation-balanced silica fiber laser," Optica **8**, 830–833 (2021).
30. Y. Zhang, J. Xu, J. Ye, *et al.*, "Ultralow-quantum-defect Raman laser based on the boson peak in phosphosilicate fiber," Photon. Res. **8**, 1155–1160 (2020).
31. Y. Zhang, S. Li, J. Ye, *et al.*, "Low quantum defect random Raman fiber laser," Opt. Lett. **47**, 1109–1112 (2022).
32. X. Ma, J. Ye, Y. Zhang, *et al.*, "Hundred-watt-level phosphosilicate Raman fiber laser with less than 1% quantum defect," Opt. Lett. **46**, 2662–2665 (2021).
33. Y. Glick, Y. Shamir, M. Aviel, *et al.*, "1.2 kW clad pumped Raman all-passive-fiber laser with brightness enhancement," Opt. Lett. **43**, 4755–4758 (2018).
34. X. Ma, J. Xu, J. Ye, *et al.*, "Cladding-pumped Raman fiber laser with 0.78% quantum defect enabled by phosphorus-doped fiber," High Power Laser Sci. Eng. **10**, e8 (2022).
35. V. R. Supradeepa, Y. Feng, and J. W. Nicholson, "Raman fiber lasers," J. Opt. **19**, 023001 (2017).
36. L. Zhang, J. Dong, and Y. Feng, "High-power and high-order random Raman fiber lasers," IEEE J. Sel. Top. Quantum Electron. **24**, 1400106 (2018).
37. S. Li, J. Xu, J. Liang, *et al.*, "Multi-wavelength random fiber laser with a spectral-flexible characteristic," Photon. Res. **11**, 159–164 (2023).
38. Y. Zhang, S. Wang, M. She, *et al.*, "Spectrally programmable Raman fiber laser with adaptive wavefront shaping," Photon. Res. **11**, 20–26 (2023).

39. I. A. Lobach, S. I. Kablukov, and S. A. Babin, "Linearly polarized cascaded Raman fiber laser with random distributed feedback operating beyond 1.5 μm," Opt. Lett. **42**, 3526–3529 (2017).
40. J. Dong, L. Zhang, J. Zhou, *et al.*, "More than 200 W random Raman fiber laser with ultra-short cavity length based on phosphosilicate fiber," Opt. Lett. **44**, 1801–1804 (2019).
41. J. Ye, C. Fan, J. Xu, *et al.*, "2-kW-level superfluorescent fiber source with flexible wavelength and linewidth tunable characteristics," High Power Laser Sci. Eng. **9**, e55 (2021).
42. M. M. Khudyakov, A. E. Levchenko, V. V. Velmiskin, *et al.*, "Narrow-linewidth diffraction-limited tapered Er-doped fiber amplifier with 2 mJ pulse energy," Photonics **9**, 933 (2022).
43. J. E. Heebner, A. K. Sridharan, J. W. Dawson, *et al.*, "High brightness, quantum-defect-limited conversion efficiency in cladding-pumped Raman fiber amplifiers and oscillators," Opt. Express **18**, 14705–14716 (2010).
44. H. Jiang, L. Zhang, and Y. Feng, "Cascaded-cladding-pumped cascaded Raman fiber amplifier," Opt. Express **23**, 13947–13952 (2015).
45. T. Qi, D. Li, Z. Wang, *et al.*, "6.85 kW ytterbium-Raman fiber amplifier based on adjustable Raman threshold method," J. Lightwave Technol. **40**, 3907–3915 (2022).
46. Y. Chen, T. Yao, H. Xiao, *et al.*, "Theoretical analysis of heat distribution in Raman fiber lasers and amplifiers employing pure passive fiber," IEEE Photon. J. **12**, 1504713 (2020).
47. H. Zhang, J. Wu, Y. Wan, *et al.*, "Kilowatt random Raman fiber laser with full-open cavity," Opt. Lett. **47**, 493–496 (2022).